Acceleration of the southern African easterly jet driven by radiative effect of biomass burning aerosols and its impact on transport during AEROCLO-sA

Jean-Pierre Chaboureau, Laurent Labbouz, Cyrille Flamant, Alma Hodzic

https://doi.org/10.5194/acp-2022-233
Preprint. Discussion started: 30 March 2022

Atmospheric Chemistry and Physics Discussions

Acceleration of the southern African easterly jet driven by radiative effect of biomass burning aerosols and its impact on transport during AEROCLO-sA

Jean-Pierre Chaboureau[1], Laurent Labbouz[1], Cyrille Flamant[2], and Alma Hodzic[3]

[1]Laboratoire d'Aérologie (LAERO), Université de Toulouse, CNRS, UPS, Toulouse, France
[2]LATMOS/IPSL, Sorbonne Université, CNRS, UVSQ, Paris, France
[3]National Center for Atmospheric Research, Boulder, CO, USA

Correspondence: Jean-Pierre Chaboureau (jean-pierre.chaboureau@aero.obs-mip.fr)

Abstract. The direct and semi-direct radiative effects of biomass burning aerosols (BBA) are investigated over southern Africa and the southeast Atlantic during the Aerosols, Radiation and Clouds in southern Africa (AEROCLO-sA) field campaign in September 2017. A reference convection-permitting simulation has been performed using the Meso-NH model with an on-line dust emission scheme, a BBA tracer emitted using the daily Global Fire Emissions Database and online-computed backward Lagrangian trajectories. The simulation captures both the aerosol optical depth and the vertical distribution of aerosols as observed from airborne and space-borne lidars. It also reproduces the occurrence of stratocumulus over the southeast Atlantic, deep convective clouds over equatorial Africa and the large-scale circulation. In contrast, a sensitivity experiment where the radiative effect of BBA is not taken into account shows the smoke plume that is predicted too low in altitude, low-cloud cover that is too weak, deep convective activity that is too frequent but not intense enough, a Benguela jet that is too strong and a southern African easterly jet that is too weak. The Lagrangian analysis indicates that BBA are transported to higher altitudes, farther southwest and with a stronger diurnal oscillation when accounting of the radiative effects of BBA. The higher smoke plume altitude can be explained by a combination of three factors: increased upward motion induced by the stronger southern African easterly jet, self-lofting of BBA and reduced subsidence associated with a less frequent deep convective activity over equatorial Africa.

1 Introduction

Biomass burning aerosols (BBA) are a major forcing agent of the regional climate over southern Africa and the southeast Atlantic during the burning season. From July to October, BBA are emitted by fires over the African continent and remain well-mixed in the boundary layer of 3 km deep on average over the source regions. They are transported by the prevailing mid-tropospheric easterly winds over the ocean, which is semi-permanently covered by an extensive stratocumulus cloud deck. Rich

https://doi.org/10.5194/acp-2022-233
Preprint. Discussion started: 30 March 2022


Atmospheric Chemistry and Physics Discussions

in black carbon that strongly absorbs solar radiation, BBA have a direct radiative effect (DRE) that changes sign depending to the underlying albedo i.e, BBA DRE is positive over highly reflective surfaces such as the stratocumulus deck and negative above low reflective surfaces such as the dark ocean. An accurate representation of the horizontal and vertical distribution of aerosol and cloud properties is therefore essential for regional climate modeling. The large spread in the sign and magnitude of the DRE as predicted by climate models has motivated several field campaign studies over the southeast Atlantic (Zuidema et al., 2016).

BBA have also a semi-direct effect by increasing air temperature, affecting atmospheric stability, changing low-level clouds and modifying the regional atmospheric circulation. Sakaeda et al. (2011) showed an increased low cloud cover over the southeast Atlantic as a response to increased lower tropospheric stability and reduced large-scale subsidence. Hodzic and Duvel (2018) found a reduction in deep convection over Borneo and water vapor convergence toward the island for moderately absorbing BBAs and an increase for more strongly absorbing BBAs. Mallet et al. (2020) showed that vertical changes in air temperature limit the subsidence over the southeast Atlantic, creating a cyclonic anomaly in the lower atmosphere. Conversely, the increase in lower troposphere stability over Angola induces an anticyclonic anomaly.

A dynamical aspect left unmentioned is the Southern African Easterly Jet (AEJ-S), a thermal wind resulting from the temperature gradient between the semi-arid region of southern Africa and the Congo Basin. Adebiyi and Zuidema (2016) analyzed BBA under strong and weak AEJ-S conditions for a 10 y period. They found that the AEJ-S speed maximum during September and October coincides with the maximum aerosol optical depth over the southern Africa and the maximum low cloud fraction over the southeast Atlantic. They also showed that the AEJ-S transports BBA more efficiently over the southeast Atlantic during strong jet episodes than during weak jet episodes. To our knowledge, the radiative effects of the BBA on the AEJ-S has not been studied to date, whereas the importance of the radiative effects of another absorbing aerosol (dust) on the northerly AEJ over West Africa has been demonstrated by Tompkins et al. (2005) and Lavaysse et al. (2011) among others.

The objective of this study is to examine the direct and semi-direct radiative effects of BBA over southern Africa and the southeast Atlantic with a particular focus on the AEJ-S. To achieve this objective, we investigate their effects using the airborne assets deployed during the AErosol, RadiatiOn, and CLOuds in southern Africa (AEROCLO-sA) field campaign (Formenti et al., 2019). From 5 to 12 September 2017, airborne lidar and dropsonde observations provided dedicated measurements of atmospheric dynamics, thermodynamics and aerosol composition. We run two convection-permitting simulations during 16 d, one with the radiative effects of BBA, the other without. Running the model without deep convection parameterization allows us to explicitly represent the vertical motions in deep convection and to calculate the trajectory of the air parcels in the updrafts and downdrafts. We compare both simulations with satellite and ground-based observations, as well as airborne lidar and dropsonde measurements. After showing that the overall realism of the simulation with radiatively-active BBA on aerosol and cloud distribution is significantly improved, we discuss the BBA radiative effects in accelerating the AEJ-S and in modifying the horizontal and vertical transport of BBA in comparison with the radiatively-inactive BBA simulation. Note that the microphysical BBA-cloud interaction (the indirect effect of BBA) is not considered here.

https://doi.org/10.5194/acp-2022-233
Preprint. Discussion started: 30 March 2022

Atmospheric Chemistry and Physics Discussions

The paper is organized as follows: Sect. 2 describes the data and the methods. Section 3 gives an overview of aerosols, clouds and dynamics during the 16 d period. Section 4 analyzes the radiative impact of BBA on radiation, temperature, dynamics and transport. Section 5 concludes the paper.

2 Data and methods

2.1 Meso-NH convection-permitting simulations

Two simulations are run with the nonhydrostatic mesoscale model Meso-NH (Lac et al., 2018), version 5.4, over a domain covering southern Africa and the southeast Atlantic (Fig. 1). The model grid has a 12 km horizontal spacing and 67 levels with a resolution of 60 m close to the surface to 600 m at high altitude. It is run for 16 d starting from 00:00 UTC 01 September 2017. The initial and lateral boundary conditions are given by operational analyses of the European Center for Medium-Range Weather Forecasts (ECMWF). Thermodynamic and other scalar variables are advected with the piece-wise parabolic method (PPM) while the momentum variables are advected with a fourth-order centered scheme coupled to an explicit fourth-order centered Runge-Kutta time splitting (Lunet et al., 2017).

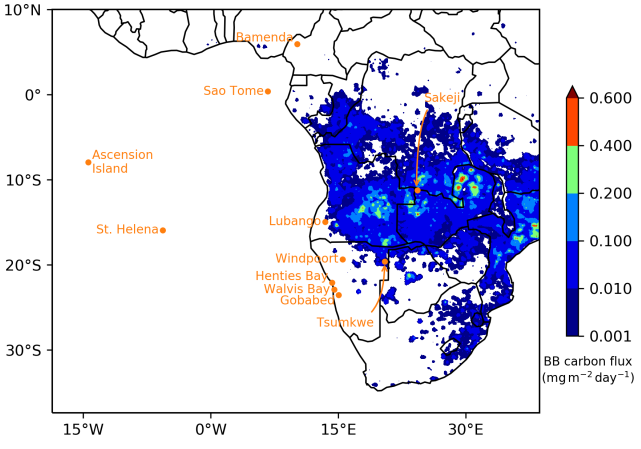

Figure 1. Meso-NH domain. The color shading shows the GFED emission of biomass burning carbon averaged between 1 and 16 September 2017.

The simulation uses the Surface Externalisée (SURFEX) scheme for surface fluxes (Masson et al., 2013), a 1.5-order closure scheme for turbulence (Cuxart et al., 2000), an eddy-diffusivity mass-flux scheme for shallow convection (Pergaud et al., 2009), the Rapid Radiative Transfer Model (Mlawer et al., 1997) for longwave radiation and the two-stream scheme (Fouquart and Bonnel, 1986) for shortwave radiation. The cloud model is the bulk microphysical scheme for mixed-phase clouds of Pinty and Jabouille (1998). In addition, a subgrid-scale scheme for cloud cover and condensate is necessary when running the model at 12 km. We use the statistical scheme of Chaboureau and Bechtold (2002) wherein the cloud cover and the cloud condensate are function of the grid-scale saturation deficit. We however do not use any deep convection parameterization in order to allow an

https://doi.org/10.5194/acp-2022-233
Preprint. Discussion started: 30 March 2022


Atmospheric Chemistry and Physics Discussions

explicit convective transport of the smoky air parcels. The aerosol model has two components. The dust scheme of Grini et al. (2006) includes the Dust Entrainment and Deposition (DEAD) scheme (Zender et al., 2003) and the ORganic and Inorganic Log-normal Aerosols Model (ORILAM) (Tulet et al., 2005), which describes the transport, dry, and wet deposition of dust. The BBA scheme includes a biomass burning carbon tracer that is emitted from the daily Global Fire Emissions Database (GFED) version 4, available at a spatial resolution of 0.25° (van der Werf et al., 2017). The BB tracer is emitted in the first vertical layer of the model, allowing its mixing by turbulence within the boundary layer. No more elaborate injection assumptions or BBA removal processes are considered here because they were found in a multimodel evaluation of BBA plume transport to play a minor role (Das et al., 2017). The two simulations differ by the radiative effect of BBA. NORAD assumes no radiative effect while BBRAD considers a mass extinction efficiency of 5.05 m^2 g^{-1} at 532 nm for BBA as used by Mallet et al. (2020) for aged smoke. The single scattering albedo is equal to 0.85. This value, which corresponds to strongly absorbing aerosols, is close to the vertical average estimated at Ascension Island (Wu et al., 2020) and over the southeastern Atlantic (Pistone et al., 2019; Cochrane et al., 2022).

The BBA transport is analyzed using the Lagrangian trajectories computed online in the model with three passive tracers (Gheusi and Stein, 2002). At each grid point of the simulation domain, the tracers are initialized with the 3-D field of their initial coordinates and advected by PPM, which conserve the mass properties of the tracers with low numerical diffusion. This allows to follow the 3-D position of each BBA tracer. Note that this approach takes into account any diabatic processes including BBA radiative heating allowing any cross-isentropic trajectory to be followed. To assess the convective activity in the simulations, synthetic brightness temperatures (BTs) at 10.8 µm are computed from the model three-hourly outputs using the radiative transfer model for the TIROS Operational Vertical Sounder (RTTOV) code (Saunders et al., 2018), implemented in Meso-NH by Chaboureau et al. (2008).

2.2 Observations

Lidar LEANDRE (Lidar Embarqué pour l'Etude des Aérosols, Nuages, Dynamique, Rayonnement et Espèces minoritaires) Nouvelle Génération (LNG, Bruneau et al., 2015) and dropsonde observations were acquired from the SAFIRE (Service des Avions Français Instrumentés pour la Recherche en Environnement) Falcon 20. The aircraft was based in Walvis Bay, located on the west coast of Namibia. Here, we use data acquired on 6 September 2017 between 07:18 and 09:12 UTC during which the Falcon 20 flew over continental Namibia prior to flying over the ocean (Formenti et al., 2019). Extinction at 532 nm is retrieved using a standard lidar inversion method that employs a lidar ratio of 70 sr, characteristic of BBA in the free troposphere (a detailed description of the inversion method is given in Chazette et al., 2019). The retrievals have an estimated uncertainty of 15 %, and a resolution of 2 km in the horizontal and 15 m in the vertical. Profiles from Vaisala dropsondes released at 08:43 and 09:08 UTC are also used.

Over the remote areas of the AEROCLO-sA domain, the vertical distribution of aerosols is assessed using the CATS (Cloud-Aerosol Transport System) lidar operated from the International Space Station (Yorks et al., 2016). CATS has flown over the simulation domain several times. We select two orbits, one over Angola and Congo on 14 September between 19:02 and

https://doi.org/10.5194/acp-2022-233
Preprint. Discussion started: 30 March 2022


Atmospheric Chemistry and Physics Discussions

19:11 UTC, the other over the southeast Atlantic on 8 September between 22:40 and 22:47 UTC. We use the CATS Level 2 Layer extinction at 1064 nm available at 60 m vertical and 5 km horizontal resolution.

Aerosol optical depth (AOD) is evaluated using the daily merged Level 3 AOD product (Deep Blue and Dark Target) from the MODIS 6.1 collection available at a spatial resolution of 1°. This product provides broad coverage by combining clear land surface (Deep Blue) retrievals with ocean and vegetated land surface (Dark Target) retrievals. We select the Aqua platform retrievals because it crosses the equator at 13:30 LT when the boundary layer is well developed. The AOD evaluation also takes advantage of the Aerosol Robotic Network (AERONET) sun photometers (Holben et al., 1998) at 10 selected stations available on the simulation domain (Ascension Island, Bamenda, St. Helena, São Tomé, Sakeji, Lubango, Henties Bay, Windpoort, Gobabeb and Tsumkwe; Fig. 1). The sun photometers provide the aerosol properties during the daytime. Here, we use the daily-mean, cloud cleared and quality assured, level 2.0 product of AOD at 532 nm, the central wavelength of the solar window.

Deep convective clouds are assessed using the BTs at 10.8 µm obtained with the Spinning Enhanced Visible and InfraRed Imager (SEVIRI) instrument aboard the geostationary satellite Meteosat Second Generation (MSG). The BTs are re-gridded from the 4 km resolution (at nadir) to the horizontal resolution of the simulations of 12 km. Following Söhne et al. (2008) among many others, deep convective clouds are defined as grid points with BTs less than 230 K. Low-level clouds are evaluated using level 3 daily product of cloud fraction and cloud top temperature from the MODIS collection 6.1 available in 1° spatial resolution. For consistency with the MODIS AOD product, we use these retrievals from the Aqua platform. The low-level cloud fraction is defined as the cloud fraction for which the cloud top temperature is greater than 273 K.

3 Overview of aerosols, clouds and dynamics

3.1 Horizontal distribution

The time variation in AOD is examined at 10 AERONET stations available on the domain (Fig. 2). In the simulations, AOD is due to BBA and dust, with the contribution of the latter shown by thin lines. Regardless of the station, the model lacks AOD at the beginning of the simulations. This is due to the time required for aerosols to be transported from the sources to the stations. Since the aerosol sources in the model are either BB or dust, both located in southern Africa, a few days are needed for the aerosols to reach the model boundaries. Note that AOD due to dust mainly affects Henties Bay and Gobabeb, and only on 3 and 4 September. Dust has hence a negligible contribution to the simulated AOD most of the time and for most stations.

The long spin-up of BBA explains the zero AOD values simulated at Ascension Island, Bamenda and St. Helena stations in the first 6 days (Fig. 2a–c). The AOD at these stations varies strongly with the simulated circulation. On the one hand, BBRAD reproduces the maximum of 0.5 on 10 September at St. Helena while it is absent in NORAD (Fig. 2c). On the other hand, NORAD overestimates the AOD at São Tomé while BBRAD simulates it in the right range (i.e., around 0.2) in the last 10 days of the simulation (Fig. 2d). In NORAD, the BBA plume extends too far north and not far enough west. At Sakeji, AOD is observed between 0.5 and 1 (Fig. 2e). Both simulations show the correct range of AOD. This suggests that the regular emission of BBA is well simulated. Near the fire source areas, Lubango and Windpoort show a stronger variation with AOD between

https://doi.org/10.5194/acp-2022-233
Preprint. Discussion started: 30 March 2022

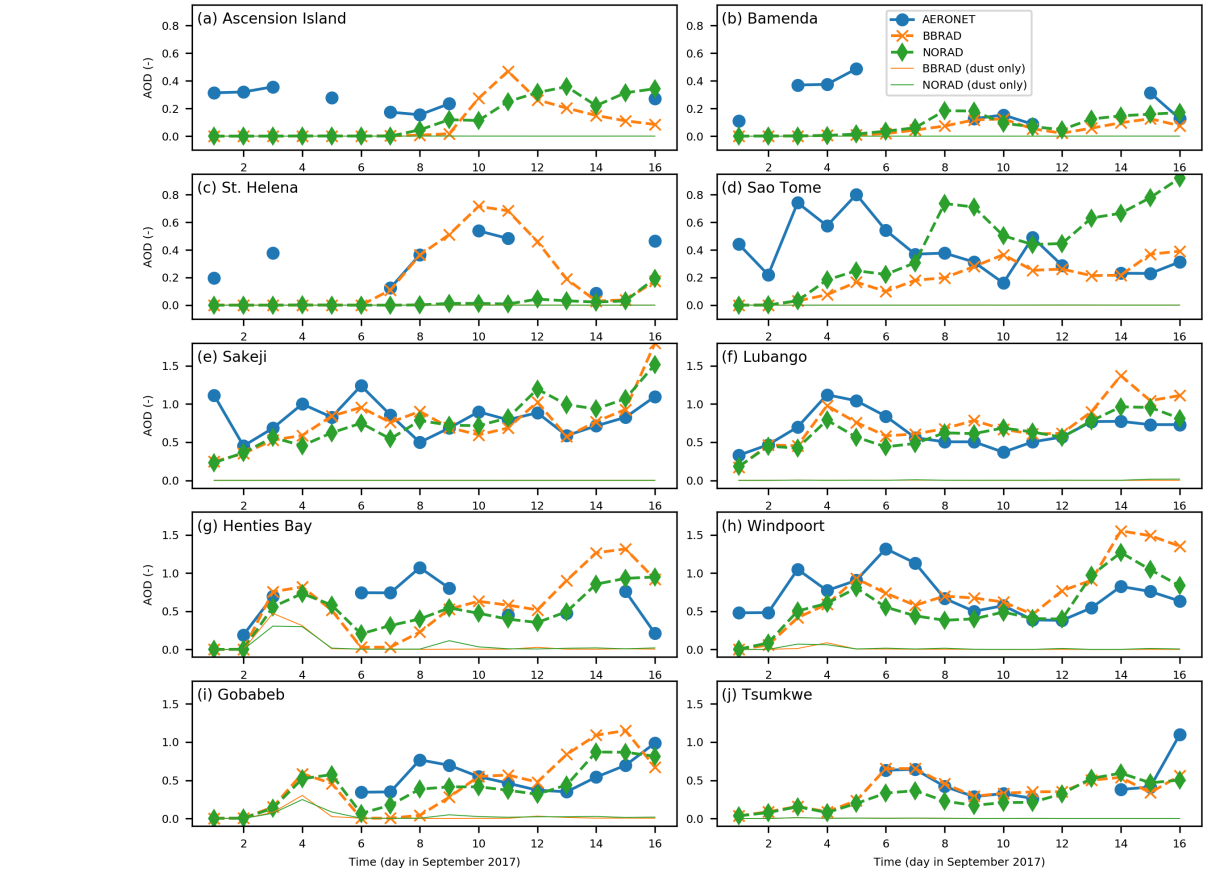

Figure 2. Time evolution of daily mean AOD between 1 and 16 September 2017 from AERONET (blue), BBRAD (orange) and NORAD (green) at **(a)** Ascension Island, **(b)** Bamenda, **(c)** St. Helena, **(d)** São Tomé, **(e)** Sakeji, **(f)** Lubango, **(g)** Henties Bay, **(h)** Windpoort, **(i)** Gobabeb and **(j)** Tsumkwe. The orange and green thin lines show the AOD due to dust for BBRAD and NORAD, respectively.

0.3 and 1.3 (Fig. 2f and h). The simulations reproduce this variation well, but underestimate the AOD peak by a few tenths. For other stations further south over Namibia (Fig. 2g–j), AOD shows less variability. It remains close to 1 at Henties Bay and around 0.5 at Gobabed and Tsumkwe. These features are fairly well reproduced by both simulations, including the short period when dust contributes to the AOD.

The simulations are further assessed in terms of horizontal distribution of AOD, low-level and deep convective clouds (Fig. 3). The fields are averaged between 8 and 16 September 2017 because of the long spin-up of BBA tracer as shown previously. They are daily averages for deep convective clouds taking advantage of frequent observations by the geostationary SEVIRI instrument and averages at 12:00 UTC for AOD and low-level clouds, a time close to the observations done by MODIS aboard the Aqua satellite. The dynamics is represented by the wind field averaged at 12:00 UTC and taken at different altitudes: 12 km corresponds to the level of maximum detrainment by deep convection over equatorial Africa; 4 km is the altitude where

https://doi.org/10.5194/acp-2022-233
Preprint. Discussion started: 30 March 2022

Atmospheric Chemistry and Physics Discussions

the AEJ-S is maximum and rapidly transports BBA; 1 km above ground level (agl) represents the low-level circulation which has an impact on the occurrence of low-level clouds.

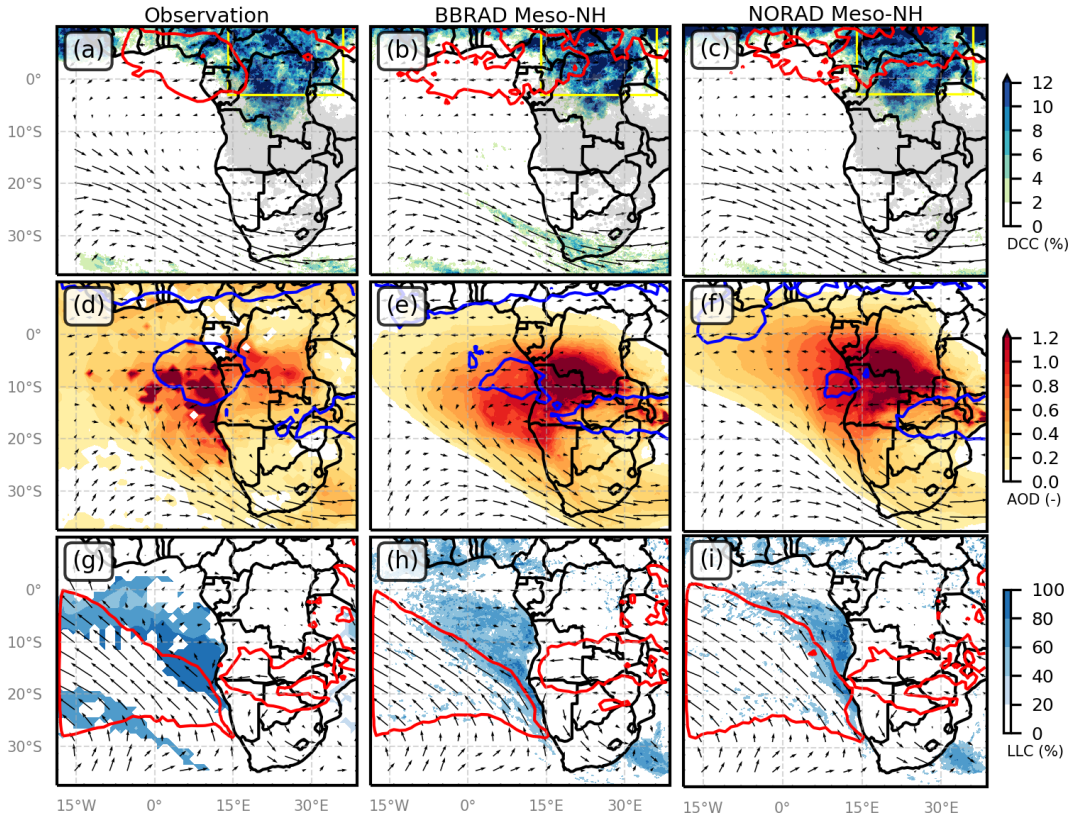

Figure 3. Top panel: occurrence of deep convective clouds from **(a)** SEVIRI, **(b)** BBRAD and **(c)** NORAD. Fire sources are shaded in grey. Middle panel: AOD from **(d)** MODIS, **(e)** BBRAD and **(f)** NORAD. Bottom panel: occurrence of low-level clouds from **(g)** MODIS, **(h)** BBRAD and **(i)** NORAD. Arrows show the winds at **(a–c)** 12 km, **(d–f)** 4 km and **(g–i)** 1 km agl from **(a, d, g)** ECMWF, **(b, e, h)** BBRAD and **(c, f, i)** NORAD. Contours show the zonal wind at **(a–c)** -12, **(d–f)** -8 and **(g–i)** $-4\,\mathrm{m\,s^{-1}}$ at 12, 4 and 1 km, respectively. Fields are averaged between 8 and 16 September 2017.

Deep convective clouds are observed mostly over the Congo Basin and north of the equator (Fig. 3a). A few events are embedded in the mid-latitude circulation south of 30° S. The simulations reproduce well the occurrence of deep convective clouds as well as the areas free of deep convection, i.e. most of the southern Africa and the southeastern Atlantic. In the observations, the occurrence of deep convective clouds equals 3.0 % over land and 7.7 % over the yellow box shown in Fig. 3a–c. NORAD is more active in deep convective clouds with 3.1 and 8.2 % of occurrence versus 2.8 and 7.7 % for BBRAD, respectively. The decrease in deep convective clouds with radiatively active BBA is a semi-direct effect discussed in Sect. 4.3. The wind at 12 km shows an anticyclonic circulation with strong westerlies over southern Africa and easterlies above $-12\,\mathrm{m\,s^{-1}}$ at the equator,

https://doi.org/10.5194/acp-2022-233
Preprint. Discussion started: 30 March 2022


Atmospheric Chemistry and Physics Discussions

along the southern fringe of the tropical easterly jet, for all three datasets. The tropical easterly jet is stronger for NORAD than for the ECMWF analysis and for BBRAD in coherence with the more active deep convection feeding it.

AOD values retrieved from MODIS observation show an arc of high values spanning over the Atlantic ocean, between 10 and 20° S and along the border between Angola and the Democratic Republic of the Congo (Fig. 3d). BBRAD reproduces this feature well, but with higher values along the border and lower values over the ocean. NORAD mimics BBRAD along the border, but misses the area over the ocean. Instead, it spans large values of AOD along the African coast up to the Gulf of Guinea. As for the wind at 12 km, the wind at 4 km shows an anticyclonic circulation with strong westerlies over southern Africa and easterlies above $-8\,\mathrm{m\,s^{-1}}$ around 10° N. Compared to the ECMWF analysis, NORAD overestimates the latter more than BBRAD. The other branch of strong easterlies around 15° S over land and 8° S over sea is the AEJ-S. BBRAD accelerates the AEJ-S compared to NORAD. It however overestimates the AEJ-S over Namibia and Tanzania with respect to ECMWF.

Low-level clouds are observed mainly over the southern Atlantic with cloud fraction up to 80 % off Namibia (Fig. 3g). Another band lies south of 20° S over the open ocean which is not simulated. Both simulations reproduce the low-level cloud cover off Namibia, but over too small an area and with too low a cloud fraction for NORAD. BBRAD mimics the observed low-level cloud cover as well as the analyzed wind field, in particular the Benguela low-level jet off Namibia. Extension too far north of the low-level jet for NORAD suggests that the dynamics inhibit the low-level cloud fraction at this location.

3.2 Vertical distribution

Two examples of the vertical distribution of extinction at 1064 nm observed by CATS are shown, one over the fire source regions on 14 September, the other over the stratocumulus region on 8 September (Fig. 4). They are compared to the extinction due to BBA and dust and to the cloud fraction from the simulations.

On 14 September, a well-mixed BBA layer with extinction value above $0.05\,\mathrm{km^{-1}}$ and a depolarization ratio less than 0.1 (not shown) is present between the ground and 5 km altitude (Fig. 4d). Above Angola, i.e. between 10 and 15° S, the layer is shallower and extinction is often constant in columns between the ground and 4 km altitude with values up to $0.25\,\mathrm{km^{-1}}$. Over the Namibian desert, i.e. around 18° S, the depth of the BBA layer increases and the extinction values decrease with altitude. Over ocean, the BBA layer is over the planetary boundary layer up to 27° S and 6 km altitude where it is topped by clouds with large extinction values. In the first 2 km altitude, aerosols are present below shallow clouds. Note that along the coast around 21° S, the strong extinction value in the first km is associated with a depolarization ratio greater than 0.5 (not shown) suggesting the presence of dust. BBRAD mimics both vertical and horizontal extinction reasonably well (Fig. 4e). Above Angola, the BBA layer is well-mixed below the approximately 316 K isentrope located at 4 km altitude. As for the observations, extinction can reach values as high as $0.25\,\mathrm{km^{-1}}$. Over Namibia, two layers are simulated, one under the 316 K isentrope and another between 320 and 324 K, that is up to 5 km altitude as observed. BBA successfully simulates the decoupling of the layer over the ocean due to the tilting of the isentropes with latitude. In the first 2 km, BBRAD well simulates a dusty cloud plume near the coast. Away from the coast, only the shallow clouds are simulated suggesting that the observed aerosol signal is neither due to BBA nor to dust, but rather to sea salt. NORAD does simulate a BBA layer sandwiched between the 304 and 320 K isentropes (Fig. 4f). However, its depth over Angola is overestimated by about 1 km and its southern extent over the ocean is limited to

https://doi.org/10.5194/acp-2022-233
Preprint. Discussion started: 30 March 2022

Atmospheric Chemistry and Physics Discussions

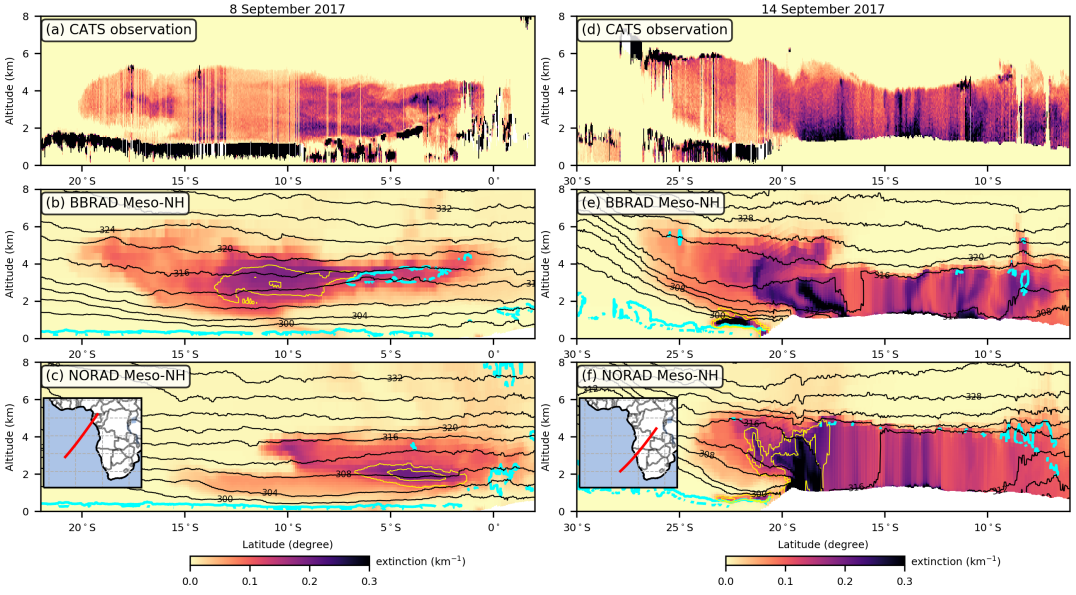

Figure 4. Vertical cross-sections of extinction at 1064 nm on **(a–c)** 8 and **(d–f)** 14 September 2017 from **(a, d)** CATS, **(b, e)** BBRAD and **(c, f)** NORAD along the red line shown in the inset of the bottom panels. In panels **(b, c, e, f)**, the black contours show the potential temperature (in K), the cyan contour the cloud fraction at 10 %, and the yellow contours the dust extinction at 0.05 and 0.1 km^{-1}. On 8 September, CATS observations were taken between 22:40 and 22:47 UTC and Meso-NH simulations are at 24:00 UTC. On 14 September, CATS observations were taken between 19:02 and 19:11 UTC and Meso-NH simulations are at 24:00 UTC.

24° S. Counter-intuitively, the heat low over Namibia is warmer and deeper for NORAD than for BBRAD. All these features can be explained by the stronger AEJ-S in BBRAD. Indeed, a stronger jet limits the vertical development of the boundary layer over Angola. It also strengthens the cyclonic circulation that weakens the heat low and exports the BBA further west, thereby limiting their direct radiative effect over land. NORAD correctly simulates the dusty cloud plume near the coast, but incorrectly fills the boundary layer between 18 and 20° S with mainly dust.

On 8 September, low-level clouds are ubiquitous along the track (Fig. 4a). Their thickness is about 500 m and their base varies from 1 km on the southern part of the track to around 500 m in its center. Between 5 and 15° S, their tops touch the BBA layer which extends up to 5 km of altitude. The BBA layer is characterized by multiple superimposed layers of few-hundred-meter thick with different extinction values (and a low depolarization ratio; not shown). The largest extinction values are north of 8° S and south of 13° S. The lower values in between suggest that BBA circulate around this area. Between 16 and 20° S, the BBA layer is 1 km above the boundary layer. BBRAD shows a BBA structure between 0 and 20° S and 1 and 6 km altitude, which is close to what is observed (Fig. 4b). The layer with high values of extinction between 5 and 10° S is however thinner than observed and the stratocumulus deck is too shallow. Interestingly, dust contributes a little to the extinction at 3 km around 8–13° S with values around 0.05 km^{-1}. NORAD misses the occurrence of elevated BBA between 15 and 20° S (Fig. 4c).

https://doi.org/10.5194/acp-2022-233
Preprint. Discussion started: 30 March 2022

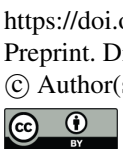

Atmospheric Chemistry and Physics Discussions

Instead, it transports BBA up to 4 km at 12° S. The stratocumulus deck is too shallow and less continuous than observed. It incorrectly simulates a heavy dusty layer between 2 and 8° S.

Another difference in the vertical distribution of aerosols between the simulations is shown for the BBA layer observed by LNG off Namibia on 6 September and on the vertical profiles of potential temperature and wind speed (Fig. 5). Note that no dust is simulated along the leg for both simulations. The BBA layer observed by LNG is a well-mixed layer between 3 and 5.5–6 km altitude (Fig. 5a). It is partially topped by shallow clouds as shown by the large extinction values. Dropsondes at 08:43 and 09:08 UTC show that the potential temperature is there almost constant with altitude, around 316 K (Fig. 5d, e). The same is true for the wind speed, around 14 m s^{-1} at 08:43 UTC and 17 m s^{-1} at 09:08 UTC (Fig. 5f, g). Over the ocean, the BBA layer is thinner and stratocumulus are found near the surface.

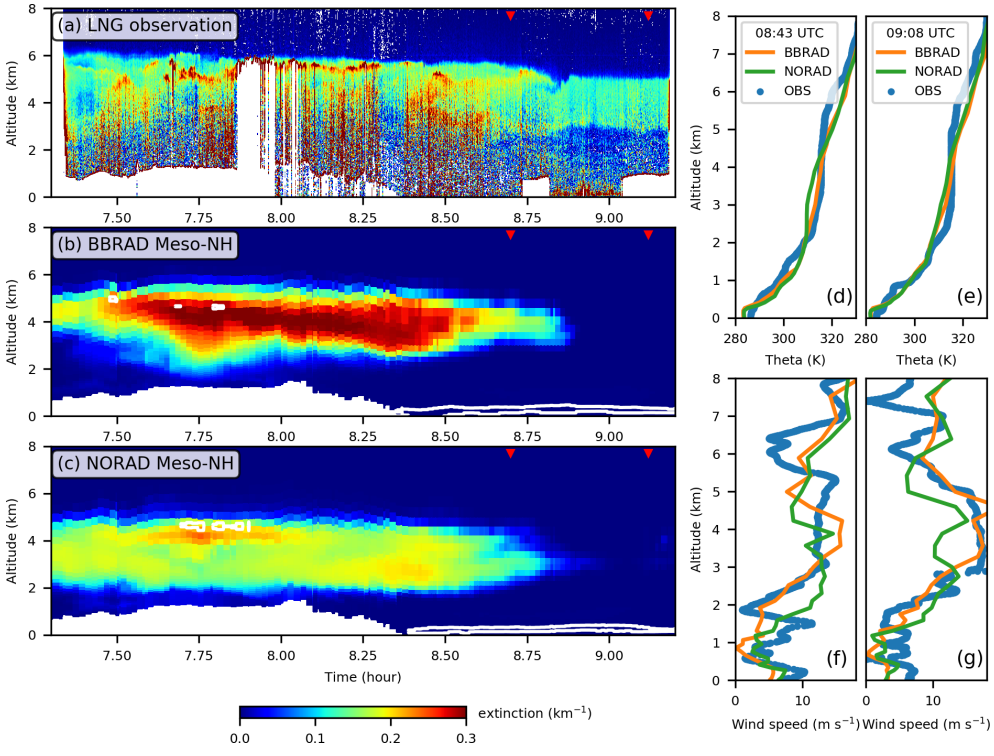

Figure 5. Left column: vertical cross-sections of extinction at 532 nm on 6 September 2017 from **(a)** LNG, **(b)** BBRAD and **(c)** NORAD along the F20 track shown in Fig. 6. LNG observations were taken between 07:18 and 09:12 UTC and Meso-NH simulations are at 09:00 UTC. the white contours show the cloud fraction at 10 %. The red triangles locate the dropsondes. Right column: profiles of **(d, e)** potential temperature and **(f, g)** wind speed from dropsondes released at **(d, f)** 08:43 and **(e, g)** 09:08 UTC, BBRAD and NORAD at 09:00 UTC.

The simulations reproduce the stratocumulus above the ocean and the BBA layer over land quite well (Fig. 5b and c). However, the thinner layer observed over the ocean (after 08:45 UTC, i.e. 8.75 h) is missing. The BBA top is also not high enough by 500 m. Therefore, the correctly but too few simulated clouds at the top of the BBA layer are too low by 500 m. This

https://doi.org/10.5194/acp-2022-233
Preprint. Discussion started: 30 March 2022

Atmospheric Chemistry and Physics Discussions

is consistent with the inversion of the potential temperature being too low by 500 m. Between 3–4 km altitude, the temperature and the wind speed are higher for BBRAD than for NORAD and closer to the observations. This is expected from the radiative effect of BBA on temperature and AEJ-S. BBRAD simulates a thinner BBA layer, which also agrees with the observations. It produces a much larger extinction than NORAD, which is somewhat overestimated.

To investigate the difference in extinction between the simulations, a sample of randomly selected back-trajectories of smoky air parcels reaching the LNG track are shown in Fig. 6. For both simulations, most of them stretch zonally between Zambia and Angola at an altitude of 3–4 km, i.e. within the AEJ-S. At the jet entrance, the area of convergence of the jet inflow is located over northern Botswana and Zimbabwe, which explains why a large part of the trajectories originate there. Another feature of interest shared by both simulations is the area of divergence of the AEJ-S in the Angola coastal region. They both show BBA at 4–5 km altitude. Indeed, the ageostrophic circulation in the jet outflow as shown by Adebiyi and Zuidema (2016) is expected to favor the passage of smoky air parcels below or above the jet level. This explains why many trajectories go up there.

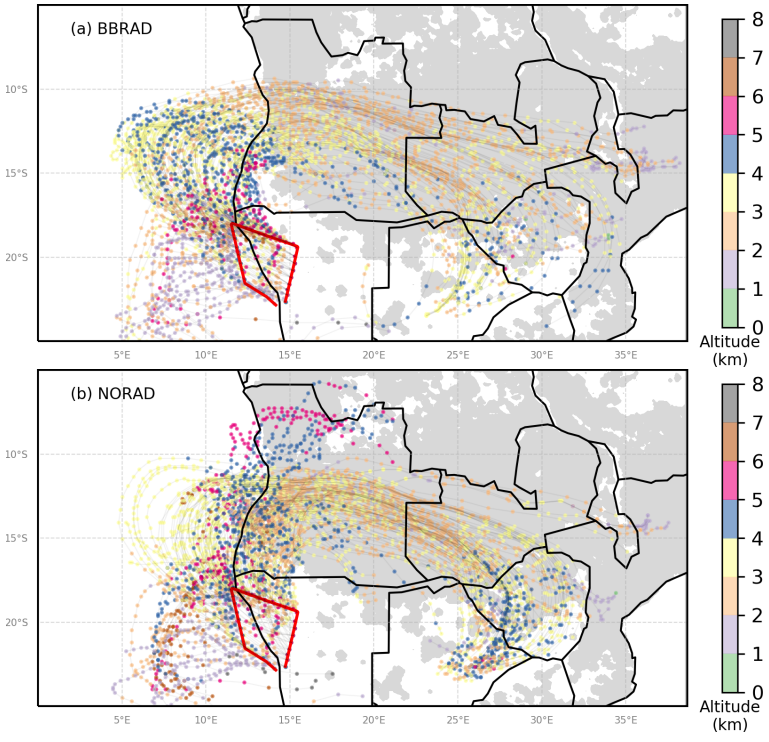

Figure 6. Selected trajectories of BB tracers ending along the LNG track (red line) at 09:00 UTC on 6 September 2017 in **(a)** BBRAD and **(b)** NORAD. Their position is indicated by dots every 3 h. Their length is 5 d and 9 h. Fire sources are shaded in grey color.

In NORAD only, the BBA that are located at 5-6 km altitude in northern Angola and then transported southward are under the dynamical forcing of the AEJ-S. In BBRAD, the track of the trajectories is narrower with more trajectories coming from the north over the continent and some going further west over the ocean. As a result, air masses with partly oceanic trajectories travel longer between the fire region and the LNG track than air masses with shorter, predominantly continental trajectories.

https://doi.org/10.5194/acp-2022-233
Preprint. Discussion started: 30 March 2022

Atmospheric Chemistry and Physics Discussions

Since the northern fire sources are more active, smoky air parcels with larger extinction values are simulated along the LNG track. In other words, a stronger AEJ-S leads to a longer pathway over fires (i.e., BBA sources) and higher extinction values in this specific case.

4 Impacts of BBA on the atmosphere

4.1 Direct effect on radiation

The direct effect of BBA on shortwave (SW) radiation and radiative heating is examined for BBRAD between 8 and 16 September (Fig. 7). It is shown as a daily mean to be discussed with results of climate models reported in the literature. The DRE is calculated as the difference between the total SW flux and the SW flux without the contribution of the BBA.

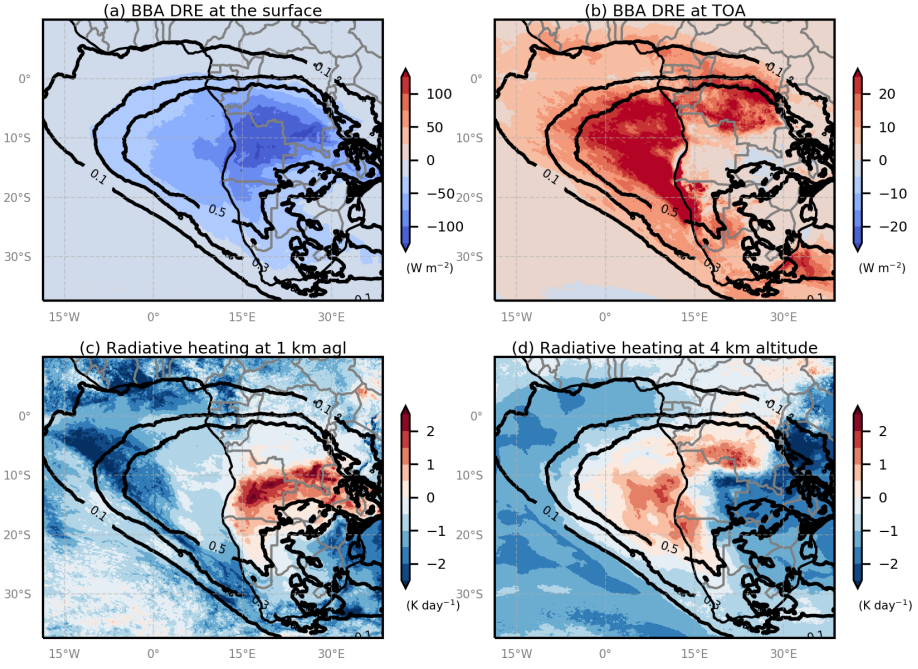

Figure 7. Results from BBRAD: BBA DRE ($\mathrm{W\,m^{-2}}$) at **(a)** the surface and **(b)** top of the atmosphere (TOA), and radiative heating ($\mathrm{K\,day^{-1}}$) at **(c)** 1 km agl and **(d)** 4 km altitude. Fields are averaged daily between 8 and 16 September 2017.

At the surface, the DRE is negative or zero everywhere (Fig. 7a). It varies with AOD, with a dimming effect of BBA as strong as $-100\,\mathrm{W\,m^{-2}}$ over and around Angola. It is 3–4 times stronger than the July-August-September averaged values of $-30\,\mathrm{W\,m^{-2}}$ reported by Mallet et al. (2020). The larger magnitude is explained by both the greater insolation and AOD in mid-September compared to seasonal values. At the top of the atmosphere, the DRE is mainly positive (Fig. 7b). It is strongest over ocean above the stratocumulus deck where it reaches a maximum of $40\,\mathrm{W\,m^{-2}}$ while it is around zero over Angola and Zambia and a small part of the Gulf of Guinea. This uneven DRE over areas of high AOD is due to the surface albedo, which is

https://doi.org/10.5194/acp-2022-233
Preprint. Discussion started: 30 March 2022


Atmospheric Chemistry and Physics Discussions

high over the oceanic stratocumulus deck and low over the land and stratocumulus-free parts of the ocean. Again, these values are 3–4 times stronger than the seasonal mean values. Furthermore, the DRE is expected to be negative over low reflectance, high AOD surfaces, i.e. over Angola and the Congo Basin, whereas near zero values are obtained here.

At 1 km agl, the radiative heating is positive over the fire source areas (Fig. 7c). It reaches a maximum of 2 K day^{-1} over central Angola and southeastern Democratic Republic of the Congo. Elsewhere, the radiative heating is negative. This is mainly a night-time cooling effect, which is the strongest over the cloud-free equatorial ocean. At 4 km altitude, the radiative heating is positive almost everywhere where the AOD is greater than 0.5, with maximum values around 1 K day^{-1} (Fig. 7d). Elsewhere, the radiative heating is negative. Over Zambia and Tanzania, the cooling that occurs just above the BBA layer is one of the strongest. Overall, the heating rates due to BBA are within the range of daily values around 1 K day^{-1} reported by Mallet et al. (2020).

4.2 Impact on dynamics

A vertical perspective along longitude is shown over ocean, across the stratocumulus deck between 5 and 10° E, and over land, across the BBA source areas between 15 and 25° E (Fig. 8). Fields are averaged at 12:00 UTC between 8 and 16 September. Examination at noon time allows an highlighting of the radiative heating in the BBA layers while excluding nighttime cooling.

Over land, the radiative heating at the BBA layer reaches a maximum value of 12 K day^{-1} at 2 km altitude around 12° S (Fig. 8b). It shows values higher than 2 K day^{-1} up to 3–4 km altitude above the fire source region between 8–22° S. This fits with the atmosphere slice with extinction higher than 0.1 km^{-1} in BBRAD (Fig. 8d). This strong heating warms the well-developed boundary-layer, lowering the 316 K isentrope to less than 4 km in altitude between 10–20° S and reinforcing the meridional contrast in potential temperature. Due to the thermal wind balance, the AEJ-S shows a core value of -10 m s^{-1} at 12° S while the associated ageostrophic circulation occurring in the entrance region of the AEJ-S induces upward motion to its north and downward motion to its south (Adebiyi and Zuidema, 2016). Self-lofting, i.e. the increase in buoyancy in the BBA layer due to radiative heating, also enhances upward motion. Because of the strong AEJ-S, the extinction is less developed vertically between 10–20° S while it has an ascending branch at about 8° S. In NORAD, the core value of the AEJ-S equals -8 m s^{-1} and the vertical motion is mainly upward in the first 8 km. The largest upward motions are in the Hadley cell north of 0° and in the boundary layer over the African highlands. It results in an extinction field almost evenly distributed vertically below the 316 K isentrope. In summary, accounting for the radiative effect of BBA changes the dynamics that feedback on the vertical distribution of BBA extinction, elevating them north of the AEJ-S.

Over ocean, the radiative heating within the BBA layer reaches a maximum value of 10 K day^{-1} at 4 km at 12° S (Fig. 8a). This value fits the SW heating rate of 9 K day^{-1} inferred from satellite observations (Deaconu et al., 2019). Located more than 1 km above the stratocumulus deck, the area of positive radiative heating overlaps the area of extinction greater than 0.2 km^{-1} in BBRAD (Fig. 8b). Such strong heating increases the temperature which lowers the 316 K isentrope to 3 km altitude at 17° S. This strengthens the meridional temperature gradient and accelerates the AEJ-S up to a core value of -10 m s^{-1} at 10° S. The ageostrophic circulation associated with the AEJ-S induces upward motions to its south and downward motions to its north

https://doi.org/10.5194/acp-2022-233
Preprint. Discussion started: 30 March 2022

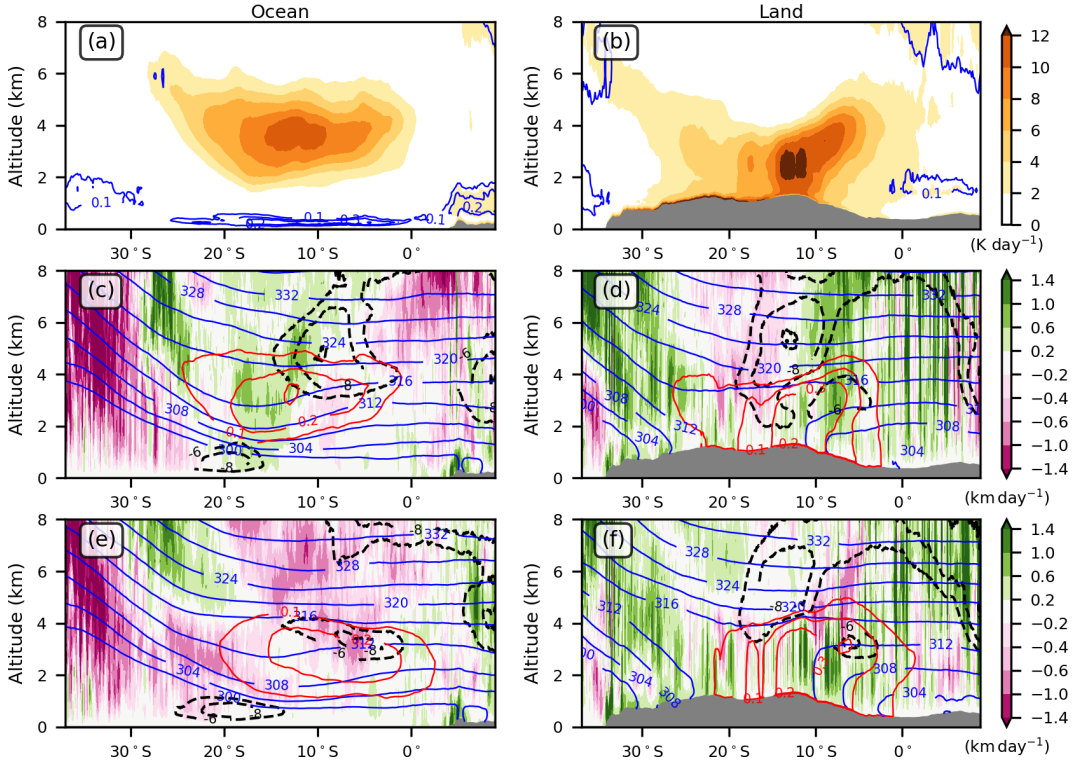

Figure 8. (a–b) Radiative heating (K day^{-1}, shading) and cloud fraction (blue contour) from BBRAD. **(c–f)** Vertical wind (m s^{-1}, shading), zonal wind (m s^{-1}, black contours when lower than -6 m s^{-1}, dotted when lower than -10 m s^{-1}), potential temperature (K, blue contours) and aerosol extinction (km^{-1}, red contours) from **(c–d)** BBRAD and **(e–f)** NORAD. Fields are averaged at 12:00 UTC between 8 and 16 September 2017 and **(a, c, e)** between 5 and 10° E and **(b, d, f)** between 15 and 25° E.

(Adebiyi and Zuidema, 2016). The self-lofting of BBA also reinforces the upward motions in the BBA layer. In NORAD, the extinction maximum of 0.2 km^{-1} is 1 km lower and 5° northward than in BBRAD (Fig. 8c). The lack of additional BBA heating in NORAD results in a much smoother meridional temperature gradient. As a consequence, the zonal wind at mid-level is weaker and lower in altitude, while the Benguala low-level jet extends in a wider meridional band around 20° S. Between 10 and 20° S, the vertical motion is upward in BBRAD and downward in NORAD. This explains why the BBA reach a higher altitude in BBRAD.

4.3 Impact on deep convection and rain

The radiative impact of BBA is shown for the temperature at 2 m, the wind at 10 m, convective available potential energy (CAPE) and the rain rate (Fig. 9). Fields are daily mean between 8 and 16 September. The difference in 2 m temperature between the two simulations is null over ocean because the sea surface temperature does not change over time for both simulations (Fig. 9a). The overall change in circulation results in a cyclonic anomaly in the wind difference at 10 m, consistent with

https://doi.org/10.5194/acp-2022-233
Preprint. Discussion started: 30 March 2022

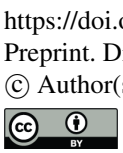

Atmospheric Chemistry and Physics Discussions

a limited northward extension of the Benguela low-level jet in BBRAD compared to NORAD. Over land, the 2 m temperature decreases where the BBA dimming seen in Fig. 7a is the strongest. It reaches −3 K over Angola and the southern part of the Democratic Republic of the Congo. This cooling effect has been reported in the literature (Mallet et al., 2020) as well as the cyclonic and anticyclonic anomalies in the wind difference at 10 m (see their Figure 11). The anticyclonic anomaly over land in Fig. 9a is not as well marked as the cyclonic circulation over the ocean, essentially due to surface friction. The 2 m temperature increases up to 1 to 2 K over land northward of 6° S. This is an aerosol forcing that feeds back on deep convection, an aerosol effect already reported, but for dust over West Africa (Tompkins et al., 2005; Chaboureau et al., 2007). Here, the anomaly prevents the low-level flow in BBRAD from extending as far northeast as it does in NORAD (compare Fig. 3h and Fig. 3i). This changes the location of the deep convective clouds by moving them to the northeast (see Fig. 3b, c).

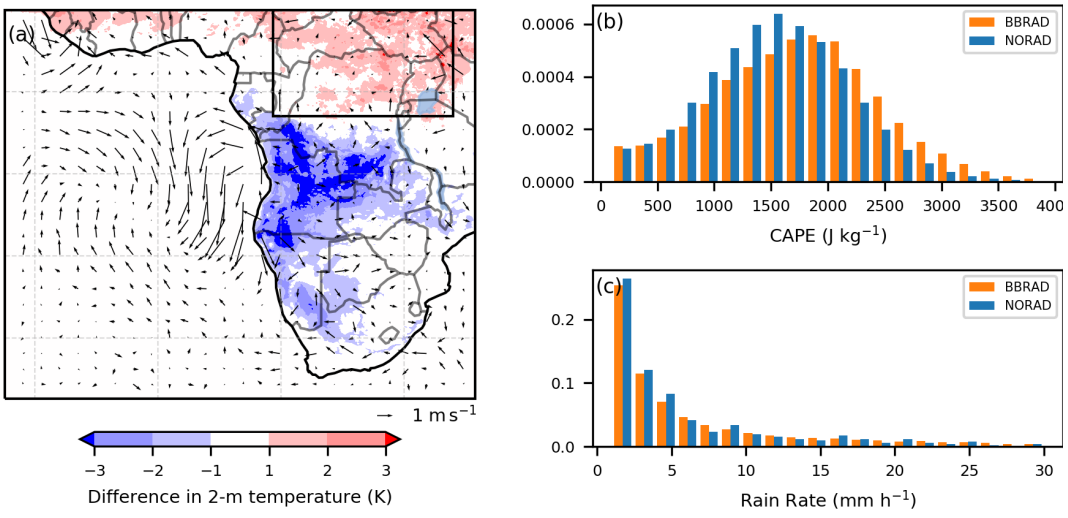

Figure 9. **(a)** Difference in 2 m-temperature (shading) and 10 m-wind (arrow) between BBRAD and NORAD. Histogram of **(b)** CAPE and **(c)** rain rate. Fields are daily mean between 8 and 16 September 2017. In panels **(b)** and **(c)**, the fields are taken from the black box over land shown in panel **(a)**. In panel **(b)**, CAPE is shown for CIN less than 1 J kg^{-1} and for CAPE larger than 100 J kg^{-1}. In panel **(c)**, the rain rate is shown for values between 1 and 30 mm h^{-1}.

Another semi-direct effect of BBA on deep convection is its intensity as shown by the CAPE and rain rate between 14–36° E and 3° S–10° N defining the black box shown in Fig. 9a. Because high temperatures are more frequent for BBRAD than for NORAD, the distribution in the most unstable CAPE varies with BBA (Fig. 9b). Following Reinares Martínez and Chaboureau (2018), CAPE is shown for convective inhibition (CIN) less than 1 J kg^{-1}. Indeed, CAPE is accessible to an air parcel if it overcomes the CIN barrier. For a CIN greater than 1 J kg^{-1}, an air parcel would have a vertical wind speed greater than 1.4 m s^{-1} below the level of free convection. In the lower levels of the atmosphere, updrafts generally do not exceed this vertical speed making the CAPE inaccessible to air parcels. As a result, around 21 % of the grid points have accessible CAPE for NORAD against 18 % for BBRAD. The larger number of grid points with accessible CAPE for NORAD explains the more frequent activity in deep convection seen in Fig. 3. Since the 2 m temperature is higher in BBRAD than in NORAD, CAPE

https://doi.org/10.5194/acp-2022-233
Preprint. Discussion started: 30 March 2022

Atmospheric Chemistry and Physics Discussions

larger than 2000 J kg^{-1} are more frequent in BBRAD. In other words, deep convection is most intense in BBRAD. However, medium values of CAPE around 1500 J kg^{-1} are more numerous in NORAD resulting in more events with rain rate above 1 and 5 mm h^{-1} (Fig. 9c). The more frequent rainfall events therefore explain why the 2 m temperature is lower in NORAD than in BBRAD in the black box shown in Fig. 9a.

4.4 Impact on transport

The radiative impact of BBA on transport is examined using the fraction of trajectories having undergone either convective or fire influences. This analysis is done over the last 7 d of the back-trajectories. Trajectories ascending by more than 3 km in 3 h at least once are considered to be under convective influence. This threshold, which is equivalent to the relatively small value of 0.3 m s^{-1}, is chosen to ensure that all convective updrafts are selected. Trajectories with BBA tracers are under fire influence if they pass over a fire region at less than 3 km altitude, i.e. within the continental boundary layer. Results are shown over the full domain and for four areas that include Ascension Island, São Tomé, St. Helena and Walvis Bay (Fig. 10). All areas have a size of 5°of longitude by 5°of latitude.

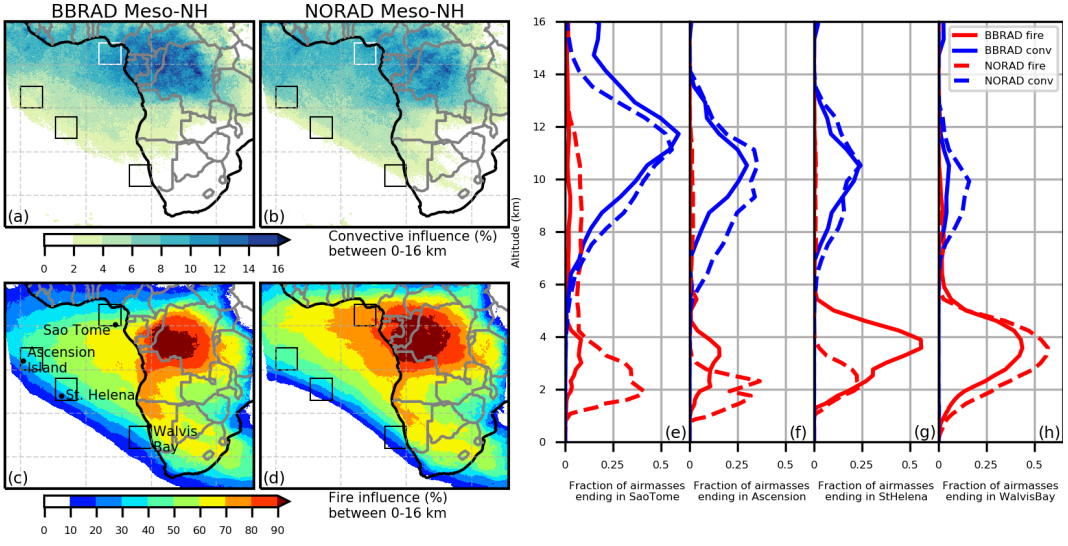

Figure 10. Left column: Fraction of air masses having **(a–b)** convective influence and **(c–d)** fire influence between 0 and 16 km in the last 7 d for **(a, c)** BBRAD and **(b, d)** NORAD. Right column: profiles of convective (blue) and fire (red) influences at **(e)** São Tomé, **(f)** Ascension, **(g)** St. Helena and **(f)** Walvis Bay areas for BBRAD (solid) and NORAD (dashed). Results are averaged from 7 d trajectories ending at 12:00 UTC every day between 8 and 16 September 2017.

The footprint of convective ascents is maximum over land in the northern part of the domain where deep convection occurs (Fig. 10a–b). The average convective influence between 0 and 16 km is greater than 16 % for both simulations. It extends over the Gulf of Guinea north of the equator within the tropical easterly jet. In the São Tomé area, the convective influence is limited to the altitude between 6 and 16 km in altitude (Fig. 10e). In consistency with a more frequent but less intense deep convective

https://doi.org/10.5194/acp-2022-233
Preprint. Discussion started: 30 March 2022

Atmospheric Chemistry and Physics Discussions

activity, it peaks at 11 km altitude in NORAD instead of 12 km in BBRAD and it is stronger below 11 km in NORAD, which explains the higher values of the vertical mean of the convective influence over the Gulf of Guinea. Over the southeast Atlantic, deep convection has a remote influence on transport. It spreads over a larger area in NORAD, which extends downstream to the eastern coasts of South Africa. Its maximum is more than 25 % at 11 km over St. Helena, up to 25 % at 10.5 km over Ascension Island and 10 % at 10 km over Walvis Bay, but only in NORAD for the latter (Fig. 10f–h). It is worth noting that the convective influence extends to lower altitudes in NORAD, which is consistent with the higher subsidence over the southeast Atlantic found previously.

The fire influence covers the northern part of the southeast Atlantic and almost the entire African landmass with a maximum of 80 % over the Republic Democratic of the Congo (Fig. 10c–d). Over the Gulf of Guinea, it reaches a vertical average of 70 % in NORAD against 50 % in BBRAD. It extends further southwest in BBRAD with a peak at 50 % at about 4 km over St. Helena against 20 % at about 2 km in NORAD (Fig. 10g). This difference between the simulations in the horizontal distribution of fire influence mimics that of the AOD, except for the amplitude. As an example, the fire influence at Walvis Bay is greater for NORAD than for BBRAD while the nearby AOD at Henties Bay is larger for BBRAD than for NORAD. Indeed, the fire influence does not account for the variability in BBA emission. Whatever the difference in amplitude, the effects due to the change in circulation remain the same: an export of BBA over the southeast Atlantic further west and at higher altitude when accounting for the radiative effect of BBA.

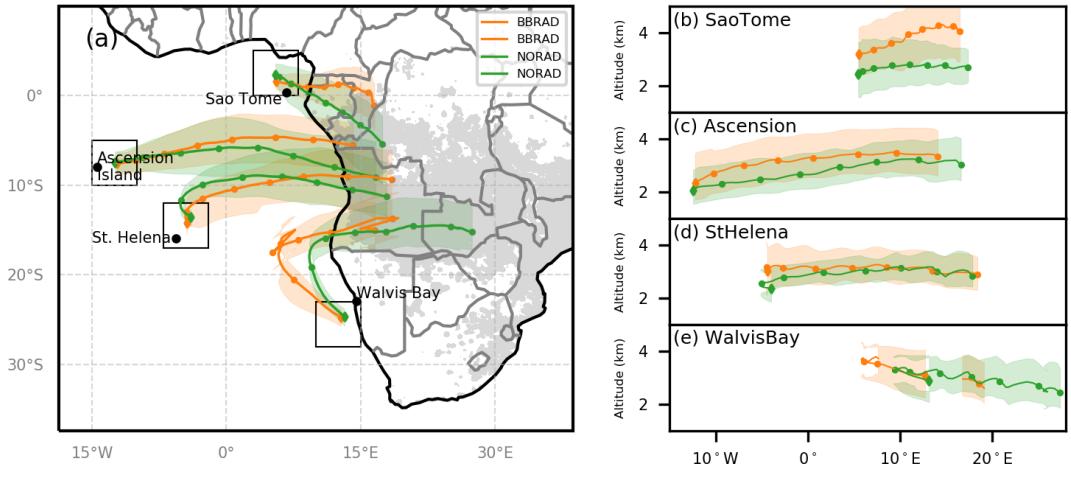

Figure 11. Back trajectories of smoky air parcels ending between 1 and 5 km in the São Tomé, Ascension, St. Helena and Walvis Bay areas. The median (bold lines, dots every 24 h, diamond at the end of the back trajectory) and the interquartile ranges (shading) are shown for BBRAD (orange) and NORAD (green). In panel **(a)**, fire sources are shaded in grey and interquartile ranges are for latitude. In panels **(b–e)**, the interquartile ranges are those of altitude. Results are averaged from 7 d trajectories ending at 12:00 UTC every day between 8 and 16 September 2017.

The pathways followed by the smoky air change if the radiative effect of BBA is taken into account. They are shown for the same four areas with median and interquartile values of the 7 d back trajectories ending between 8 and 16 September at

https://doi.org/10.5194/acp-2022-233
Preprint. Discussion started: 30 March 2022


Atmospheric Chemistry and Physics Discussions

12:00 UTC (Fig. 11). Observing a single time of day highlights diurnal oscillations along the trajectories that peak during the day (Fig. 11b–e). This is due to the radiative effect experienced by the smoky air parcels. During the night, they cool down and descend. During the day, they heat up and ascend. Since the radiative heating is stronger for radiatively active BBA in BBRAD, the solar forcing causes a higher elevation and thus, a stronger diurnal oscillation.

Another effect of radiatively active BBA is that the trajectories of smoky air parcels ending at São Tomé, Ascension and St. Helena are higher in BBRAD than in NORAD (Fig. 11b–d). The average difference along the 7 d travel is 1190, 380, 250 and 260 m, respectively. This is consistent with the fire influence peaking at higher altitude at these locations. As a result of the stronger AEJ-S, their pathways have a more westward direction in BBRAD than in NORAD and have a more northerly origin (Fig. 11a). The stronger AEJ-S has a more dramatic impact on the trajectories ending at Walvis Bay (Fig. 11a). It transports BBA further west in BBRAD before being redirected to the southeast. As a result, the origin of BBA reaching the Walvis Bay area after 7 d of transport is Angola in BBRAD and Zambia in NORAD. The increased long-range transport of BBA is consistent with the faster and higher trajectories observed during strong jet events compared to weak jet events in the climatological study of Adebiyi and Zuidema (2016).

5 Conclusions

The direct and semi-direct effects of BBA over southern African and the southeast Atlantic is addressed during the AEROCLO-sA campaign in September 2017 with the use of two convection-permitting simulations, one taking into account the BBA radiative effect and the other not. Their effects on the transport are also discussed using the Meso-NH online Lagrangian trajectory tool activated in both simulations.

The realism of both simulations is assessed against satellite, airborne and ground-based observations and ECMWF analyzes. The BBRAD simulation reproduces well the horizontal and vertical distribution of BBA as well as the temporal evolution of the AOD, at least for a 7 d period for the stations located far from the fire sources, namely São Tomé, Ascension Island and St. Helena. The location of the stratocumulus deck off Angola and the deep convective activity over equatorial Africa is also well captured. In contrast, the NORAD simulation produces a BBA plume extending too far north, not far enough west and southwest and not high enough over the stratocumulus deck, a low-level cloud cover extending too far south and a deep convective activity more frequent and less intense than in BBRAD. The superiority of the simulation with BBA radiative effect and the strong effects induced by its deactivation allow a clear assessment of their impact on dynamics and transport.

The direct radiative effect due to BBA is globally well simulated. At the surface, the dimming effect lowers the temperature by -3 K over Angola and the southern part of the Democratic Republic of Congo (while the sea surface temperature is prescribed in the simulations). At the top of the atmosphere, the direct radiative effect is strongest over the BBA layer covering a high albedo surface, mainly the stratocumulus deck and the Congo forest. A daily average heating rate of more than 1 K day^{-1} is simulated in the continental boundary layer of the fire zone and in the BBA layer over the ocean at 4 km altitude.

The first semi-direct effect is the acceleration of the AEJ-S. Due to the BBA radiative heating of the air above Angola and the Democratic Republic of the Congo, the meridional gradient of the temperature increases over land which in turn accelerates

https://doi.org/10.5194/acp-2022-233
Preprint. Discussion started: 30 March 2022


Atmospheric Chemistry and Physics Discussions

the AEJ-S due to thermal wind balance. The stronger AEJ-S moves the boundary between the stratocumulus deck and the Benguala low-level jet further south. A second semi-direct effect is the change in vertical circulation. The motion is upward over Angola and over the stratocumulus deck instead of downward when radiative effects are cut off. This can be explained by a combination of three causes: ageostrophic upward motion induced by the stronger AEJ-S; self-lofting of BBA; and reduced subsidence associated with less frequent deep convective activity over equatorial Africa.

Another radiative semi-direct effect of BBA less studied in the literature is a modification of the BBA transport. As shown with 7 d back-trajectories, it is found that their pathway is shifted by a few hundred kilometers, northward or westward depending on their final destination. This change considerably their areas of origin. Another result is that their transport altitude is a few hundred meters higher when the radiative effect of BBA is taken into account. This is because, by gaining heat by solar absorption during the day, they increase the potential temperature of the air in which they reside. In other words, BBA do not experience isentropic motions. Therefore, care must be taken when using Lagrangian trajectories along isentropes to study origin and transport of BBA.

Despite a rather coarse representation of BBA and their radiative effect in our simulations, our results suggest a significant impact on the dynamics, thermodynamics and composition of the atmosphere in southern Africa. Further studies with Meso-NH will investigate the sensitivity of the simulations to a more sophisticated representation of BBA and their optical and radiative properties, as well as their impact on regional dynamics and cloud distribution over land and ocean. The significance of our results on the role of BBA radiative effects on the AEJ-S, will also be compared to longer climatological periods using climate simulations with and without BBA radiative forcing.

Data availability. The LNG lidar data is available via the digital object identifier (DOI): 10.6096/AEROCLO.1774 and the dropsondes data via DOI: 10.6096/AEROCLO.1777. The AERONET data were downloaded from the NASA AERONET website (http://aeronet.gsfc.nasa.gov/, last access: March 2022), the MODIS data from the Giovanni web portal (http://disc.sci.gsfc.nasa.gov/giovanni, last access: March 2022) and the SEVIRI and CATS data from ICARE (https://www.icare.univ-lille.fr/, last access: March 2022). The Meso-NH-derived fields and back trajectories data can be obtained upon request to the corresponding author of the paper.

Author contributions. LL and JPC performed the simulations and the analyses. JPC prepared the manuscript with contributions from all co-authors.

Competing interests. The authors declare that they have no conflict of interest.

Special issue statement. This article is part of the special issue “New observations and related modelling studies of the aerosol–cloud–climate system in the Southeast Atlantic and southern Africa regions (ACP/AMT inter-journal SI)”. It is not associated with a conference

https://doi.org/10.5194/acp-2022-233
Preprint. Discussion started: 30 March 2022

Atmospheric Chemistry and Physics Discussions

Acknowledgements. Computer resources for running Meso-NH were allocated by GENCI through Project 90569. We thank the PIs Brent Holben, Jens Redemann, Carlos Ribeiro, Nichola Knox, Stuart Piketh, and their staff for establishing and maintaining the AERONET sites used in this investigation. JPC thanks NCAR/ACOM for the visitor grant. LL received a CNES postdoctoral fellowship.

https://doi.org/10.5194/acp-2022-233
Preprint. Discussion started: 30 March 2022

Atmospheric Chemistry and Physics Discussions

References

Adebiyi, A. A. and Zuidema, P.: The role of the southern African easterly jet in modifying the southeast Atlantic aerosol and cloud environments, Quart. J. Roy. Meteor. Soc., 142, 1574–1589, https://doi.org/10.1002/qj.2765, 2016.

Bruneau, D., Pelon, J., Blouzon, F., Spatazza, J., Genau, P., Buchholtz, G., Amarouche, N., Abchiche, A., and Aouji, O.: 355-nm high spectral resolution airborne lidar LNG: system description and first results, Appl. Opt., 54, 8776–8785, https://doi.org/10.1364/AO.54.008776, 2015.

Chaboureau, J.-P. and Bechtold, P.: A simple cloud parameterization derived from cloud resolving model data: diagnostic and prognostic applications, J. Atmos. Sci., 59, 2362–2372, https://doi.org/10.1175/1520-0469(2002)059<2362:ASCPDF>2.0.CO;2, 2002.

Chaboureau, J.-P., Tulet, P., and Mari, C.: Diurnal cycle of dust and cirrus over West Africa as seen from Meteosat Second Generation satellite and a regional forecast model, Geophys. Res. Lett., 34, L02 822, https://doi.org/10.1029/2006GL027771, 2007.

Chaboureau, J.-P., Söhne, N., Pinty, J.-P., Meirold-Mautner, I., Defer, E., Prigent, C., Pardo, J.-R., Mech, M., and Crewell, S.: A midlatitude cloud database validated with satellite observations, J. Appl. Meteor. Climatol., 47, 1337–1353, https://doi.org/10.1175/2007JAMC1731.1, 2008.

Chazette, P., Flamant, C., Totems, J., Gaetani, M., Smith, G., Baron, A., Landsheere, X., Desboeufs, K., Doussin, J.-F., and Formenti, P.: Evidence of the complexity of aerosol transport in the lower troposphere on the Namibian coast during AEROCLO-sA, Atmos. Chem. Phys., 19, 14 979–15 005, https://doi.org/10.5194/acp-19-14979-2019, 2019.

Cochrane, S. P., Schmidt, K. S., Chen, H., Pilewskie, P., Kittelman, S., Redemann, J., LeBlanc, S., Pistone, K., Segal Rozenhaimer, M., Kacenelenbogen, M., Shinozuka, Y., Flynn, C., Ferrare, R., Burton, S., Hostetler, C., Mallet, M., and Zuidema, P.: Biomass burning aerosol heating rates from the ORACLES (ObseRvations of Aerosols above CLouds and their intEractionS) 2016 and 2017 experiments, Atmos. Meas. Tech., 15, 61–77, https://doi.org/10.5194/amt-15-61-2022, 2022.

Cuxart, J., Bougeault, P., and Redelsperger, J.-L.: A turbulence scheme allowing for mesoscale and large-eddy simulations, Quart. J. Roy. Meteor. Soc., 126, 1–30, https://doi.org/10.1002/qj.49712656202, 2000.

Das, S., Harshvardhan, H., Bian, H., Chin, M., Curci, G., Protonotariou, A. P., Mielonen, T., Zhang, K., Wang, H., and Liu, X.: Biomass burning aerosol transport and vertical distribution over the South African-Atlantic region, J. Geophys. Res., 122, 6391–6415, https://doi.org/10.1002/2016JD026421, 2017.

Deaconu, L. T., Ferlay, N., Waquet, F., Peers, F., Thieuleux, F., and Goloub, P.: Satellite inference of water vapour and above-cloud aerosol combined effect on radiative budget and cloud-top processes in the southeastern Atlantic Ocean, Atmos. Chem. Phys., 19, 11 613–11 634, https://doi.org/10.5194/acp-19-11613-2019, 2019.

Formenti, P., D'Anna, B., Flamant, C., Mallet, M., Piketh, S. J., Schepanski, K., Waquet, F., Auriol, F., Brogniez, G., Burnet, F., Chaboureau, J.-P., Chauvigné, A., Chazette, P., Denjean, C., Desboeufs, K., Doussin, J.-F., Elguindi, N., Feuerstein, S., Gaetani, M., Giorio, C., Klopper, D., Mallet, M. D., Nabat, P., Monod, A., Solmon, F., Namwoonde, A., Chikwililwa, C., Mushi, R., Welton, E. J., and Holben, B.: The Aerosols, Radiation and Clouds in southern Africa (AEROCLO-sA) field campaign in Namibia: overview, illustrative observations and way forward, Bull. Amer. Meteo. Soc., 100, 1277–1298, https://doi.org/10.1175/BAMS-D-17-0278.1, 2019.

Fouquart, Y. and Bonnel, B.: Computations of solar heating of the Earth's atmosphere: A new parametrization, Beitr. Phys. Atmos., 53, 35–62, 1986.

Gheusi, F. and Stein, J.: Lagrangian description of airflows using Eulerian passive tracers, Quart. J. Roy. Meteor. Soc., 128, 337–360, https://doi.org/10.1256/00359000260498914, 2002.

https://doi.org/10.5194/acp-2022-233
Preprint. Discussion started: 30 March 2022

Atmospheric Chemistry and Physics Discussions

Grini, A., Tulet, P., and Gomes, L.: Dusty weather forecasts using the MesoNH mesoscale atmospheric model, J. Geophys. Res., 111, D19205, https://doi.org/10.1029/2005JD007007, 2006.

Hodzic, A. and Duvel, J. P.: Impact of Biomass Burning Aerosols on the Diurnal Cycle of Convective Clouds and Precipitation Over a Tropical Island, J. Geophys. Res., 123, 1017–1036, https://doi.org/https://doi.org/10.1002/2017JD027521, 2018.

Holben, B., Eck, T., Slutsker, I., Tanré, D., Buis, J., Setzer, A., Vermote, E., Reagan, J., Kaufman, Y., Nakajima, T., Lavenu, F., Jankowiak, I., and Smirnov, A.: AERONET—A federated instrument network and data archive for aerosol characterization, Remote Sensing of Environment, 66, 1–16, https://doi.org/10.1016/S0034-4257(98)00031-5, 1998.

Lac, C., Chaboureau, J.-P., Masson, V., Pinty, J.-P., Tulet, P., Escobar, J., Leriche, M., Barthe, C., Aouizerats, B., Augros, C., Aumond, P., Auguste, F., Bechtold, P., Berthet, S., Bieilli, S., Bosseur, F., Caumont, O., Cohard, J.-M., Colin, J., Couvreux, F., Cuxart, J., Delautier, G., Dauhut, T., Ducrocq, V., Filippi, J.-B., Gazen, D., Geoffroy, O., Gheusi, F., Honnert, R., Lafore, J.-P., Lebeaupin Brossier, C., Libois, Q., Lunet, T., Mari, C., Maric, T., Mascart, P., Mogé, M., Molinié, G., Nuissier, O., Pantillon, F., Peyrillé, P., Pergaud, J., Perraud, E., Pianezze, J., Redelsperger, J.-L., Ricard, D., Richard, E., Riette, S., Rodier, Q., Schoetter, R., Seyfried, L., Stein, J., Suhre, K., Thouron, O., Turner, S., Verrelle, A., Vié, B., Visentin, F., Vionnet, V., and Wautelet, P.: Overview of the Meso-NH model version 5.4 and its applications, Geosci. Model Dev., 11, 1929–1969, https://doi.org/10.5194/gmd-11-1929-2018, 2018.

Lavaysse, C., Chaboureau, J.-P., and Flamant, C.: Dust impact on the West African heat low in summertime, Quart. J. Roy. Meteor. Soc., 137, 1227–1240, https://doi.org/10.1002/qj.844, 2011.

Lunet, T., Lac, C., Auguste, F., Visentin, F., Masson, V., and Escobar, J.: Combination of WENO and Explicit Runge–Kutta Methods for Wind Transport in the Meso-NH Model, Mon. Weather Rev., 145, 3817 – 3838, https://doi.org/10.1175/MWR-D-16-0343.1, 2017.

Mallet, M., Solmon, F., Nabat, P., Elguindi, N., Waquet, F., Bouniol, D., Sayer, A. M., Meyer, K., Roehrig, R., Michou, M., Zuidema, P., Flamant, C., Redemann, J., and Formenti, P.: Direct and semi-direct radiative forcing of biomass-burning aerosols over the southeast Atlantic (SEA) and its sensitivity to absorbing properties: a regional climate modeling study, Atmos. Chem. Phys., 20, 13 191–13 216, https://doi.org/10.5194/acp-20-13191-2020, 2020.

Masson, V., Le Moigne, P., Martin, E., Faroux, S., Alias, A., Alkama, R., Belamari, S., Barbu, A., Boone, A., Bouyssel, F., Brousseau, P., Brun, E., Calvet, J.-C., Carrer, D., Decharme, B., Delire, C., Donier, S., Essaouini, K., Gibelin, A.-L., Giordani, H., Habets, F., Jidane, M., Kerdraon, G., Kourzeneva, E., Lafaysse, M., Lafont, S., Lebeaupin Brossier, C., Lemonsu, A., Mahfouf, J.-F., Marguinaud, P., Mokhtari, M., Morin, S., Pigeon, G., Salgado, R., Seity, Y., Taillefer, F., Tanguy, G., Tulet, P., Vincendon, B., Vionnet, V., and Voldoire, A.: The SURFEXv7.2 land and ocean surface platform for coupled or offline simulation of earth surface variables and fluxes, Geosci. Model Dev., 6, 929–960, https://doi.org/10.5194/gmd-6-929-2013, 2013.

Mlawer, E. J., Taubman, S. J., Brown, P. D., Iacono, M. J., and Clough, S. A.: Radiative transfer for inhomogeneous atmospheres: RRTM, a validated corrolated-k model for the longwave, J. Geophys. Res., 102D, 16 663–16 682, https://doi.org/10.1029/97JD00237, 1997.

Pergaud, J., Masson, V., Malardel, S., and Couvreux, F.: A Parameterization of Dry Thermals and Shallow Cumuli for Mesoscale Numerical Weather Prediction, Bound. Layer. Meteor., 132, 83–106, https://doi.org/10.1007/s10546-009-9388-0, 2009.

Pinty, J.-P. and Jabouille, P.: A mixed-phase cloud parameterization for use in a mesoscale non-hydrostatic model: simulations of a squall line and of orographic precipitations, in: Conf. on cloud physics, Everett, WA, Amer. Meteor. Soc., pp. 217–220, 1998.

Pistone, K., Redemann, J., Doherty, S., Zuidema, P., Burton, S., Cairns, B., Cochrane, S., Ferrare, R., Flynn, C., Freitag, S., Howell, S. G., Kacenelenbogen, M., LeBlanc, S., Liu, X., Schmidt, K. S., Sedlacek III, A. J., Segal-Rozenhaimer, M., Shinozuka, Y., Stamnes, S., van Diedenhoven, B., Van Harten, G., and Xu, F.: Intercomparison of biomass burning aerosol optical properties from in situ and remote-sensing instruments in ORACLES-2016, Atmos. Chem. Phys., 19, 9181–9208, https://doi.org/10.5194/acp-19-9181-2019, 2019.

https://doi.org/10.5194/acp-2022-233
Preprint. Discussion started: 30 March 2022

Reinares Martínez, I. and Chaboureau, J.-P.: Precipitation and Mesoscale Convective Systems: Radiative Impact of Dust over Northern Africa, Mon. Weather Rev., 146, 3011–3029, https://doi.org/10.1175/MWR-D-18-0103.1, 2018.

Sakaeda, N., Wood, R., and Rasch, P. J.: Direct and semidirect aerosol effects of southern African biomass burning aerosol, J. Geophys. Res., 116, https://doi.org/10.1029/2010JD015540, 2011.

Saunders, R., Hocking, J., Turner, E., Rayer, P., Rundle, D., Brunel, P., Vidot, J., Roquet, P., Matricardi, M., Geer, A., Bormann, N., and Lupu, C.: An update on the RTTOV fast radiative transfer model (currently at version 12), Geosci. Model Dev., 11, 2717–2737, https://doi.org/10.5194/gmd-11-2717-2018, 2018.

Söhne, N., Chaboureau, J.-P., and Guichard, F.: Verification of cloud cover forecast with satellite observation over West Africa, Mon. Weather Rev., 136, 4421–4434, https://doi.org/10.1175/2008MWR2432.1, 2008.

Tompkins, A. M., Cardinali, C., Morcrette, J.-J., and Rodwell, M.: Influence of aerosol climatology on forecasts of the African Easterly Jet, Geophys. Res. Lett., 32, L10 801, https://doi.org/10.1029/2004GL022189, 2005.

Tulet, P., Crassier, V., Cousin, F., Suhre, K., and Rosset, R.: ORILAM, a three-moment lognormal aerosol scheme for mesoscale atmospheric model: Online coupling into the Meso-NH-C model and validation on the Escompte campaign, J. Geophys. Res., 110, D18201, https://doi.org/10.1029/2004JD005716, 2005.

van der Werf, G. R., Randerson, J. T., Giglio, L., van Leeuwen, T. T., Chen, Y., Rogers, B. M., Mu, M., van Marle, M. J. E., Morton, D. C., Collatz, G. J., Yokelson, R. J., and Kasibhatla, P. S.: Global fire emissions estimates during 1997–2016, Earth Syst. Sci. Data, 9, 697–720, https://doi.org/10.5194/essd-9-697-2017, 2017.

Wu, H., Taylor, J. W., Szpek, K., Langridge, J. M., Williams, P. I., Flynn, M., Allan, J. D., Abel, S. J., Pitt, J., Cotterell, M. I., Fox, C., Davies, N. W., Haywood, J., and Coe, H.: Vertical variability of the properties of highly aged biomass burning aerosol transported over the southeast Atlantic during CLARIFY-2017, Atmos. Chem. Phys., 20, 12 697–12 719, https://doi.org/10.5194/acp-20-12697-2020, 2020.

Yorks, J. E., McGill, M. J., Palm, S. P., Hlavka, D. L., Selmer, P. A., Nowottnick, E. P., Vaughan, M. A., Rodier, S. D., and Hart, W. D.: An overview of the CATS level 1 processing algorithms and data products, Geophys. Res. Lett., 43, 4632–4639, https://doi.org/10.1002/2016GL068006, 2016.

Zender, C. S., Bian, H., and Newman, D.: Mineral Dust Entrainment and Deposition (DEAD) model: Description and 1990s dust climatology, J. Geophys. Res., 108(D14), 4416, https://doi.org/10.1029/2002JD002775, 2003.

Zuidema, P., Redemann, J., Haywood, J., Wood, R., Piketh, S., Hipondoka, M., and Formenti, P.: Smoke and Clouds above the Southeast Atlantic: Upcoming Field Campaigns Probe Absorbing Aerosol's Impact on Climate, Bull. Amer. Meteo. Soc., 97, 1131 – 1135, https://doi.org/10.1175/BAMS-D-15-00082.1, 2016.